Bioactive Materials 17 (2022) 221–233

Contents lists available at ScienceDirect

Bioactive Materials

journal homepage: www.keaipublishing.com/en/journals/bioactive-materials

Tumor cell membrane-camouflaged responsive nanoparticles enable MRI-guided immuno-chemodynamic therapy of orthotopic osteosarcoma

Liwen Fu [a], Weiying Zhang [c], Xiaojun Zhou [a], Jingzhong Fu [b,**], Chuanglong He [a,*]

[a] State Key Laboratory for Modification of Chemical Fibers and Polymer Materials, College of Chemistry, Chemical Engineering and Biotechnology, Donghua University, Shanghai, 201620, China
[b] Department of Thoracic Oncology, Jiujiang Cancer Hospital, Jiangxi Province, China
[c] Health Management Center, Shandong Provincial Hospital Affiliated to Shandong First Medical University, Jinan, 250021, China

ARTICLE INFO

Keywords:
Ginsenoside Rh2
Hollow manganese dioxide
Magnetic resonance imaging
Chemodynamic therapy
Immunotherapy

ABSTRACT

Osteosarcoma is a refractory bone disease in young people that needs the updating and development of effective treatment. Although nanotechnology is widely applied in cancer therapy, poor targeting and inadequate efficiency hinder its development. In this study, we prepared alendronate (ALD)/K7M2 cell membranes-coated hollow manganese dioxide ($HMnO_2$) nanoparticles as a nanocarrier to load Ginsenoside Rh2 (Rh2) for Magnetic Resonance imaging (MRI)-guided immuno-chemodynamic combination osteosarcoma therapy. Subsequently, the ALD and K7M2 cell membranes were successively modified on the surface of $HMnO_2$ and loaded with Rh2. The tumor microenvironment (TME)-activated Rh2@$HMnO_2$-AM nanoparticles have good bone tumor-targeting and tumor-homing capabilities, excellent GSH-sensitive drug release profile and MRI capability, and attractive immuno-chemodynamic combined therapeutic efficiency. The Rh2@$HMnO_2$-AM nanoparticles can effectively trigger immunogenic cell death (ICD), activate $CD4^+$/$CD8^+$ T cells *in vivo*, and upregulate BAX, BCL-2 and Caspase-3 in cellular level. Further results revealed that Rh2@$HMnO_2$-AM enhanced the secretion of IL-6, IFN-γ and TNF-α in serum and inhibited the generation of $FOXP3^+$ T cells (Tregs) in tumors. Moreover, the Rh2@$HMnO_2$-AM treatment significant restricted tumor growth *in-situ* tumor-bearing mice. Therefore, Rh2@$HMnO_2$-AM may serve as an effective and bio-friendly nanoparticle platform combined with immunotherapy and chemodynamic therapy to provide a novel approach to osteosarcoma therapy.

1. Introduction

Malignant bone tumors frequently occur in the group of children or adolescents, accompanied with other complicated complications (such as bone fractures or hypercalcaemia), which is hard to cure and causes great pain to patients [1,2]. Osteosarcoma belonged to malignant bone tumor is characterized by striking local aggressivity and unexpected early systemic metastasis tendency [3,4]. Although various therapeutic methods (including surgery and adjuvant chemotherapy) have been applied in recent years, only patients with early-stage osteosarcoma could be cured via surgical resection [5,6]. Surgery can remove directly the tumor section, while it cannot inhibit tumor invasion and recurrence caused by osteosarcoma. Although the combination of surgery and traditional chemotherapy has achieved the five-year survival rate, the drug resistance of osteosarcoma has restricted the combined therapeutic efficacy [7,8]. Therefore, it is worthwhile to develop a novel nanotechnology-based diagnose and treatment strategy for osteosarcoma therapy.

Immunotherapy has attracted widely attention on cancer treatment which concentrates on triggering the immune response to restrict tumor growth, exhibiting a promising strategy of rationally using powerful "elite troops" from organism itself for efficient cancer treatment [9]. Cancer immunotherapy approximately classified into two strategies: stimulating some essential factors related to immune system (such as cytokines therapy, cancer vaccines) and immune checkpoint-blockade (ICB) [9]. In particular, immunogenic cell death (ICD) is a typical process caused mainly by two pathways: ICD inducers (including anthracyclines, microtubule-destabilizing agents, cardiac glycosides, etc) and

Peer review under responsibility of KeAi Communications Co., Ltd.
* Corresponding author.
** Corresponding author.
E-mail address: hcl@dhu.edu.cn (C. He).

https://doi.org/10.1016/j.bioactmat.2022.01.035
Received 1 December 2021; Received in revised form 11 January 2022; Accepted 19 January 2022
Available online 26 January 2022

dying cancer cells (bring the tumor-specific immune response) [9]. However, single immunotherapy generally has the some clinical barriers such as high costs, unexpected individual difference reflected by various types of clinically tumors [10]. Thus, some other cancer treatments (chemotherapy, photodynamic therapy, radiotherapy, chemodynamic therapy, etc) can improve the efficiency of immunotherapy. For example, Fu and co-workers constructed a $CoFe_2O_4$ nanoflower applied on augmented sonodynamic/chemodynamic combination therapy for the enhancement of immune responses [11]. Hu et al. developed 1-MT-Pt-PPDA@MoS_2 nanosystems for the combined chemo/-photothermal treatment-mediated immunogenic cell death (ICD) and the 1-MT-induced immune checkpoint blockade [12]. Ginsenoside is a kind of sterol compound, which is regarded as the active ingredient in ginseng. Ginsenoside can be divided into several types, including Rh2, Rh3, Rg1, Rg2, Rg3, etc. These ingredients play an effective role in the treatment of some diseases. For example, Rg1 can recover fatigue, improve memory and delay aging. Rg2 has anti-shock effect and prevent coronary heart disease. Ginsenoside Rh2 monomer can inhibit the growth of cancer cells, induce the apoptosis of tumor cells, reverse the abnormal differentiation of tumor cells and improve immunity and other functions [13,14], which is more effective against highly metastatic osteosarcomas. Thus, we chose Rh2 as the immune activator in nanosystem. Zhang and co-workers found that ginsenosides Rh2 regulates well on intramorumoral permeation and the therapeutic efficiency of doxorubicin by interfering with the expression of p-glycoprotein (P-gp) [15]. The toxicity of ginsenoside Rh2 to some normal cells or tissues is almost negligible even at very high concentrations [16]. However, natural and unprocessed ginsenosides have macromolecule structure that is difficult to be absorbed by the body after oral administration, which limits the utilization of ginsenoside Rh2 [17]. Some researchers have also proposed solutions to the poor bioavailability of ginsenosides. Hu et al. used *o*-carboxymethyl chitosan nanoparticles to load ginsenosides Rh2 by ionic crosslinking to improve the water solubility of ginsenosides Rh2 [18]. Ling and co-workers designed celastrol-PEG-G Rh2 nanoparticles by modifying PEG with ginsenoside Rh2 and celastrol to achieve the synergistic therapy of lung cancer [19]. Thus, it is worth considering that more ingenious nano-carrier can be utilized for effective ginsenoside Rh2 delivery. In addition, ginsenoside has some inhibitory effect on tumors, but limitations remain the therapeutic effect when used alone. The combination of Rh2 with chemotherapeutic agents significantly improves antitumor efficiency and reduces the side effects of monotherapy use [20].

Chemodynamic therapy (CDT), utilizing Fenton or Fenton-like reaction for in situ cancer treatments, was firstly proposed by Bu's group [21]. CDT not only expands the application of Fenton reaction, but also avoids normal tissue toxicity to some degree for further valuable clinical translation. The selection of effective CDT nanoagents plays an essential role in optimizing the CDT effect, which needs to be considered from all kinds of aspects including the modulation of tumor microenvironment (TME) and the assistance of some exogenous factors [22]. TME, which is generally characterized by vascular abnormalities, low pH values and hypoxia, has a negative effect on therapeutic outcomes in various cancer therapies [23,24]. An increasing number of TME-triggered drug delivery systems (DDSs) have been developed to realize tumor-specific cancer therapy due to the interesting features mentioned above [25,26]. Moreover, it has been proposed that regulating the TME in solid tumors can enhance significantly cancer therapy efficiency, which exhibits establishing TME-regulating nanoscale DDSs may be of significant interests for cancer therapy [27,28]. Manganese dioxide (MnO_2)-based nanoparticles have been widely studied as a powerful weapon against cancer due to its unique TME-responsive feature, which are able to react with H^+, GSH or H_2O_2 to realize visualization (the generated Mn^{2+} ions are able to enhance T1-MR imaging contrast *in vivo*) and "greenization" (Fenton-like reaction) [29–31]. In comparison to previously reported MnO_2 nanosystems, hollow manganese oxide ($HMnO_2$) nanomaterials have larger cavities and better loading capacity, which attracts substantial attention as TME-activated drug delivery systems (DDS) [32–36].

Tumor cell membrane-camouflaged nanoparticles have been obtaining increased attention on cancer treatment ascribe to their virtue of excellent biocompatibility, immune escaping, tumor targeting specificity, prolonged circulation and enhanced pharmacokinetic profile [37,38]. For example, Shen et al. developed a cancer cell membrane camouflaged black-titanium nanoparticles which were functionalized with Iridium complexes for hierarchical targeted synergistic sonodynamic/NIR–II–guided photothermal cancer imaging and therapy. The nanosystems exhibited the ability to form efficiently heat upon NIR-II irradiation as well as catalytically generate reactive oxygen species upon ultrasound radiation [39]. Chen and co-workers prepared a tumor-associated macrophage (TAM) membrane-coated upconversion nanoparticle for photodynamic immunotherapy of tumor. The NPR@TAMM nanosystems could accumulate in TME due to the tumor-homing effect and immune compatibility, reduce in CSF1 levels in serum and restricting of CSF1/CSF1R signaling for the suppression of tumor growth and metastasis [40]. Various cancer cell membranes have been proved to endow nanoparticles the homotypic recognition to the corresponding cell lines owing to the existence of specific proteins (integrin, focal adhesion kinase, RHO family proteins, etc) in the phospholipid bilayer on nanoparticles surface [41–45]. Thus, K7M2 cell-derived membranes can endow nanoparticles with specific tumor-homing capability to homologous osteosarcoma *in vivo*. It is the first time that our group has utilized K7M2 cell membrane as a compass towards osteosarcoma to increase the delivery efficacy of nanosystems.

Herein, we constructed a TME-activated hollow MnO_2 nanoparticle, which loaded ginsenosides Rh2, modified with alendronate (ALD) and coated with K7M2 cancer cell membrane (M). This nanoplatform can not only stimulate innate immunity and adaptive immunity *in vivo*, but trigger the Fenton-like reaction (between Mn^{2+} and excess H_2O_2 in TME) simultaneously in situ osteosarcom. The Hollow MnO_2 nanoparticles were functionalized with ALD/K7M2 cancer cell membrane (AM), and further encapsulated ginsenosides Rh2 as immune-activators, obtaining Rh2@$HMnO_2$-AM nanoparticles. The resulting Rh2@$HMnO_2$-AM efficiently integrates Mn^{2+}-mediated MRI imaging capability and bone-targeted immuno-chemodynamic combination osteosarcoma therapy into one. Upon internalization of Rh2@$HMnO_2$-AM nanoparticles by K7M2 cells, the hollow MnO_2 framework consumed intracellular antioxidant GSH underwent a redox reaction with GSH to yield glutathione disulfide (GSSG) and Mn^{2+}. Furthermore, the released Mn^{2+} transform endogenous H_2O_2 generated from mitochondria into therapeutic ·OH. The GSH consumed by MnO_2 is aim to prevent ·OH scavenging and ensure a continuous supply for intensified efficient cancer CDT. We systematically investigated the morphology, structure, colloidal stability and the ginsenosides Rh2 delivery performance of Rh2@$HMnO_2$-AM, and explored their K7M2 cells target ability as well as *in vitro* Fenton-like effect. Moreover, the activation of immature DC cells (DCs) by ginsenosides Rh2 and the distribution of $CD4^+$/$CD8^+$ T cells both in tumor and spleen regions, and immuno-chemodynamic combination osteosarcoma therapy *in-situ* tumor animal model were assessed.

2. Experimental section

2.1. Materials and Reagents

Tetraethyl orthosilicate (TEOS), poly(allylamine hydrochloride) (PAH, Mw ≈ 15000), polyacrylic acid (PAA, Mw ≈ 1800) and manganese (II) chloride ($MnCl_2$) were obtained from Sigma-Aldrich. Alendronate (ALD) was obtained from Sangon Biotech. Potassium permanganate ($KMnO_4$) and sodium carbonate (Na_2CO_3) were purchased from Sinopharm Chemical Reagent Co., Ltd. Ginsenoside Rh2 was purchased from Chengdu Must Bio-technology Co., Ltd. (Chengdu, China).

K7M2 cell, Human umbilical vein endothelial cell (HUVEC) and mouse leukaemic monocyte macrophage cell line (RAW 264.7) were

purchased from the Chinese Academy of Science (Shanghai, China). Penicillin−streptomycin, trypsin, Fetal bovine serum (FBS) Dulbecco's Modified Eagle Medium (DMEM) and Roswell Park Memorial Institute (RPMI) 1640 medium were obtained from Gibco Life Technologies Co. (Grand Island, NY). Cell Counting Kit-8 (CCK-8) was purchased from the Beyotime Institute of Biotechnology (Shanghai, China). Calcein-AM, propidium iodide (PI), 4′,6-diamidino-2-phenylindole (DAPI) and 2′,7′-dichlorofluorescein diacetate (DCFH-DA) were obtained from BestBio Biotechnology Co., Ltd. (Shanghai, China). Anti-GAPDH rabbit polyclonal antibody (pAb), anti-calreticulin (CRT) rabbit pAb, anti-high mobility group protein (HMGB-1) rabbit pAb, anti-CD8 alpha rabbit pAb, anti-CD3-phycoerythrin (anti-CD3-PE), anti-CD8-fluorescein isothiocyanate (anti-CD8-FITC), anti-CD80 PE, anti-CD86 FITC and IgG isotype control were obtained from eBioscience (Shanghai, China).

2.2. Synthesis of solid silica nanospheres ($sSiO_2$)

The synthetic process was based on previous method with some modifications [46]. 500 μL of $NH_3{\cdot}H_2O$, 14 mL ethanol and 2 mL of DI water were vigorously stirred at 50 °C for 20 min. Next, 0.5 mL TEOS was dropwise introduced into the above solution and meanwhile the mixture was stirred (150 rpm) continuously under 50 °C for 1.5 h. The as-prepared $sSiO_2$ was purified and dispersed in DI water.

2.3. Synthesis of $HMnO_2$-PAH/PAA

The layer of MnO_2 coated on the $sSiO_2$ was obtained by mixing the solution of $KMnO_4$ and as-made $sSiO_2$, which imitates the reported method [28]. In order to obtain the hollow structure, the core of $sSiO_2$ should be removed by incubating $sSiO_2$-MnO_2 nanoparticles with Na_2CO_3 solution at 50 °C for 12 h. The obtained $HMnO_2$ nanoparticles were isolated and washed with DI water for three times by centrifugation at 11963×*g* for 10 min. The obtained $HMnO_2$ above was dispersed in 5 mL of H_2O, then was added into 5 mL PAH solution (5 mg/mL) under ultrasonication and stirring for 3 h, collected and washed with DI water until the supernatant becomes colorless and transparent. The prepared $HMnO_2$-PAH was dropwisely introduced into 5 mL PAA solution (5 mg/mL) under ultrasonication and stirring for 3 h, finally washing and collecting for further use.

2.4. Synthesis of $HMnO_2$-AM

Alendronate was connected with $HMnO_2$-PAH/PAA by the usage of common EDC/NHS method [47]. EDC/NHS was dissolved in PBS, adjusting the pH of solution to 5.0 and kept stirring for 1 h, followed by regulating the pH to 7.4 with NaOH for the conjugation of Alendronate onto $HMnO_2$-PAH/PAA. Subsequently, 3 mg Alendronate was dissolved in 3 mL PBS, and then was added to above $HMnO_2$-PAH/PAA solution and keep stirring for 24 h under room temperature. The obtained $HMnO_2$-PAH/PAA-ALD was purified by DI water for several times.

To prepare tumor cell membrane coated $HMnO_2$-AM, the mixture of $HMnO_2$-PAH/PAA-ALD and K7M2 cell membrane was extruded through a polycarbonate membrane (with 200 nm pores) via the usage of liposome extruder and repeated for 11 times, following by centrifugation at 11963×*g* for 15 min to obtain the $HMnO_2$-AM nanoparticles.

2.5. Characterization

The prepared nanoparticles were studied with TEM operated on the voltage of 200 kV with a LaB_6 electron gun (JEM-2100, JEOL Ltd., Japan). Element mappings were acquired using field-emission transmission electron microscopy (Talos F200S). The Fourier transform infrared (FTIR) spectra were recorded on a Nexus 670 (Thermo Nicolet, USA) spectrometer and examined by KBr pellets. Dynamic light scattering (DLS) was used to estimate the size distribution of the nanoparticles using a BI-200SM multiangle dynamic/static laser scattering instrument (Brookhaven, U.S.). UV–vis spectra measurement was examined by a Jasco V530 UV–vis spectrophotometer (Jasco, Japan).

2.6. pH and GSH-dependent degradation and drug release kinetics

Rh2@$HMnO_2$-AM nanoparticles were dispersed in PBS at pH 7.4 or 6.5 with or without various concentration of GSH (0 or 2 mM). The samples were measure by the usage of UV–vis spectrometer to determine the extent of degradation. For Rh2 loading, 20 mg $HMnO_2$-AM nanoparticles were dispersed in 20 mL absolute ethanol under ultrasonic vibration until the nanoparticles are uniformly dispersed. 1 mL Rh2 aqueous solution (2 mg/mL) was mixed with above $HMnO_2$-AM dispersion, the mixture was stirred at room temperature for 24 h and then washed with PBS for several times to remove the extra Rh2 that was not fully loaded (the supernatant of the mixture was collected together).

In order to evaluate the *in vitro* Rh2 release behavior of Rh2@$HMnO_2$-AM, 5 mg Rh2@$HMnO_2$-AM nanoparticles were dispersed in 1 mL of PBS (pH 7.4 or 6.5, GSH = 0 or 2 mM) and put into a dialysis bag (MWCO = 3500 Da), fully soaked in 9 mL of PBS (similar with the inside of dialysis bag) and set at 37 °C with shaking (280 rpm). 1 mL of external sample solution was collected at predetermined time points and supplied with an equal volume of fresh medium. The concentration of the Rh2 released was determined via HPLC-ELSD according to previous method [48].

2.7. Assessment of chemodynamic process of Rh2@$HMnO_2$-AM

The mixture of 10 μg/mL MB, 8 mM H_2O_2, 0.5 mM $MnCl_2$ and 25 mM $NaHCO_3$/5% CO_2 buffer solution was placed inside a shaker at 37 °C for 0.5 h. Methylene blue (MB) is utilized as an indicator of ·OH due to its ability of adsorb oxidizing ·OH. Thus, the resulting MB degradation was monitored via UV–vis spectrophotometer (665 nm).

In order to assess the effect of GSH on chemodynamic process of Rh2@$HMnO_2$-AM, the degradation of MB caused by Mn^{2+}-guided Fenton reaction was evaluated in the absence of GSH or presence of different concentrations of GSH (1, 2, 4, 10 mM). In detail, the mixture of GSH, 10 μg/mL MB, 8 mM H_2O_2, Rh2@$HMnO_2$-AM ([Mn] = 0.5 mM), and 25 mM $NaHCO_3$/5% CO_2 buffer was incubated at 37 °C for 0.5 h, then centrifuged to obtain the supernatant and measuring via UV–vis spectrophotometer. In addition, the MB degradation caused by different concentrations of nanoparticles (0, 1, 2, 4, 10 mM) was further measured to verify the chemodynamic activity of Rh2@$HMnO_2$-AM.

2′, 7′-dichlorofluorescin diacetate (DCFH-DA) probe was generally utilized for tracing ROS through oxidation processes (the oxidation product is fluorescence dichlorofluorescein), thus was selected to measure the intracellular ·OH production. K7M2 cells were cultured in DMEM medium containing 10% (v/v) fetal bovine serum, 1% penicillin and 1% streptomycin in a humidified atmosphere (37 °C and 5% CO_2) and were seeded in 24-well plates under 5% CO_2 at 37 °C for 24 h. Subsequently, the medium was removed and different componence ($MnCl_2$ or Rh2@$HMnO_2$-AM, [Mn] = 20 μg/mL) was added and incubated overnight. Then, the cells were washed for twice with PBS, followed by DCFH-DA solution was added for another 30 min-incubation. Finally, the ROS production was observed and fluorescence images were obtained via an inverted fluorescence microscopy.

2.8. Cytotoxicity assay and cellular uptake evaluation of Rh2@$HMnO_2$-AM

The cytotoxicity of Rh2@$HMnO_2$-AM was assessed by CCK-8 assay. Firstly, three types of cells (K7M2, RAW 264.7, HUVEC) were cultured in 96-well plates at a density of 10^4 cells per cell until cells grew adherence. Next, a series of concentrations (200, 100, 50, 25, 12.5, 0 μg/mL) of Rh2@$HMnO_2$-AM were co-cultured with cells for 24 h and 48 h, respectively. Subsequently, the DMEM medium in every well were removed and washed gently with PBS for twice (be careful not to flush

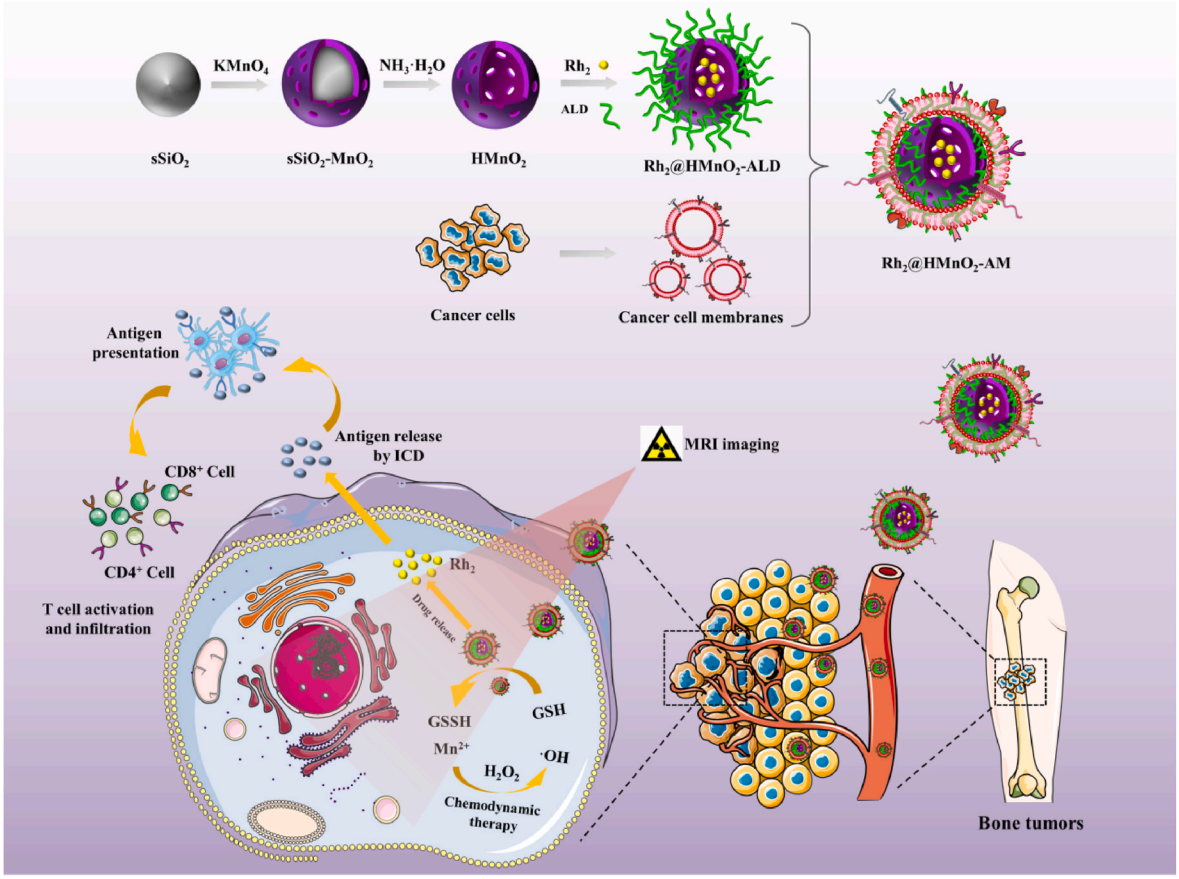

Scheme 1. Synthetic procedure of Rh2@$HMnO_2$-AM and mechanism of MRI-guided immuno-chemodynamic synergistic osteosarcoma therapy.

the cells down when washed with PBS). Furthermore, the cells were cultured in as-prepared CCK-8 solution for 2 h to detect the absorption value at 450 nm using the a microplate reader for obtaining the optical density (OD) that reflect the relative cell viability.

The Rh2 was replaced with doxorubicin (DOX) as a marker for observing the distribution of DOX@$HMnO_2$-AM in K7M2 cells and RAW264.7 cells**.** Then, K7M2 cells or RAW264.7 cells were seeded in Confocal Dishes (10^6 cells per dish) by over-night culture, then 50 μg/mL DOX@$HMnO_2$ or DOX@$HMnO_2$-AM was added and co-incubated for 3 h. Before test, the unabsorbed nanoparticles were washed with PBS for three times, following by 4% paraformaldehyde fixed solution was added under 4 °C for 1 h. Subsequently, the excess paraformaldehyde was sucked out and DAPI dye was utilized to observe under CLSM.

2.9. DC cells activation in transwell co-culture model

Murine bone-marrow-derived DCs were obtained from C57BL/6 mice according to the established protocols [49,50]. Firstly, bone marrow was obtained from the tibias and femurs of mice. A red blood cell lysis buffer was used to lyse red blood cells for extracting DCs, then washing three times and resuspending in prepared RPMI 1640 medium containing 5 ng/mL of GM-CSF and 5 ng/mL of IL-4. After 48 h of incubation in six-well cell culture plates, adherent cells were collected while non-adherent cells were removed and further culturing for a week. Subsequently, non-adherent cells were immature DCs (iDCs) and were collected for further treatments.

A transwell co-culture system was utilized to investigate the activation and Rh2@$HMnO_2$-AM mediation of DCs maturation *in vitro*. Briefly, K7M2 cells were cultured in the upper layer of transwell and DCs were harvest in the lower layer. After cells adhere to the wall, the K7M2 cells in the upper layer were treated via different treatments (PBS, $HMnO_2$-AM, Rh2, Rh2@$HMnO_2$, Rh2@$HMnO_2$-AM). The groups treated with PBS were regarded as the control. After 48 h of co-culture, DCs in the lower layer were collected, then staining with antibodies of PE-CD80 and FITC-CD86 for flow-cytometry analysis.

2.10. Western blot assay in vitro

In order to assess the immunogenic cell death (ICD) of K7M2 cells after different treatments, 6-well plates were used to seed K7M2 cells (about 2×10^5 cells per well) with right amount of DMEM medium and incubate overnight at 37 °C/5% CO_2. Next, K7M2 cells in each well were added with 2 mL DMEM medium containing Rh2@$HMnO_2$-AM. After culturing for 24 h, K7M2 cells were washed three times with neutral PBS and centrifuged. Then, 0.3 mL of lysis buffer containing phenylmethanesulfonyl fluoride was added to cells and cultured in 0 °C for 30 min. Subsequently, the cell lysates were measured by the usage of Western blot assay to explore the HMGB1 protein expression [51]. Moreover, we evaluated the possible therapeutic mechanism of Rh2@$HMnO_2$-AM nanoparticles by the usage of Western blot assay, such as the expression of BAX, BCL-2, Caspase 3.

2.11. In vivo distribution

Animal experiments were performed in accordance with local animal welfare laws and guidelines of the Donghua University and approved by the Animal Ethics Committee of Donghua University (Approval No. 2020–0018). To assess the *in vivo* distribution of $HMnO_2$-AM, Cy-5 is usually chosen as an effective reactive dye to mark amino groups of some organics (such as peptides, proteins and oligonucleotides). In

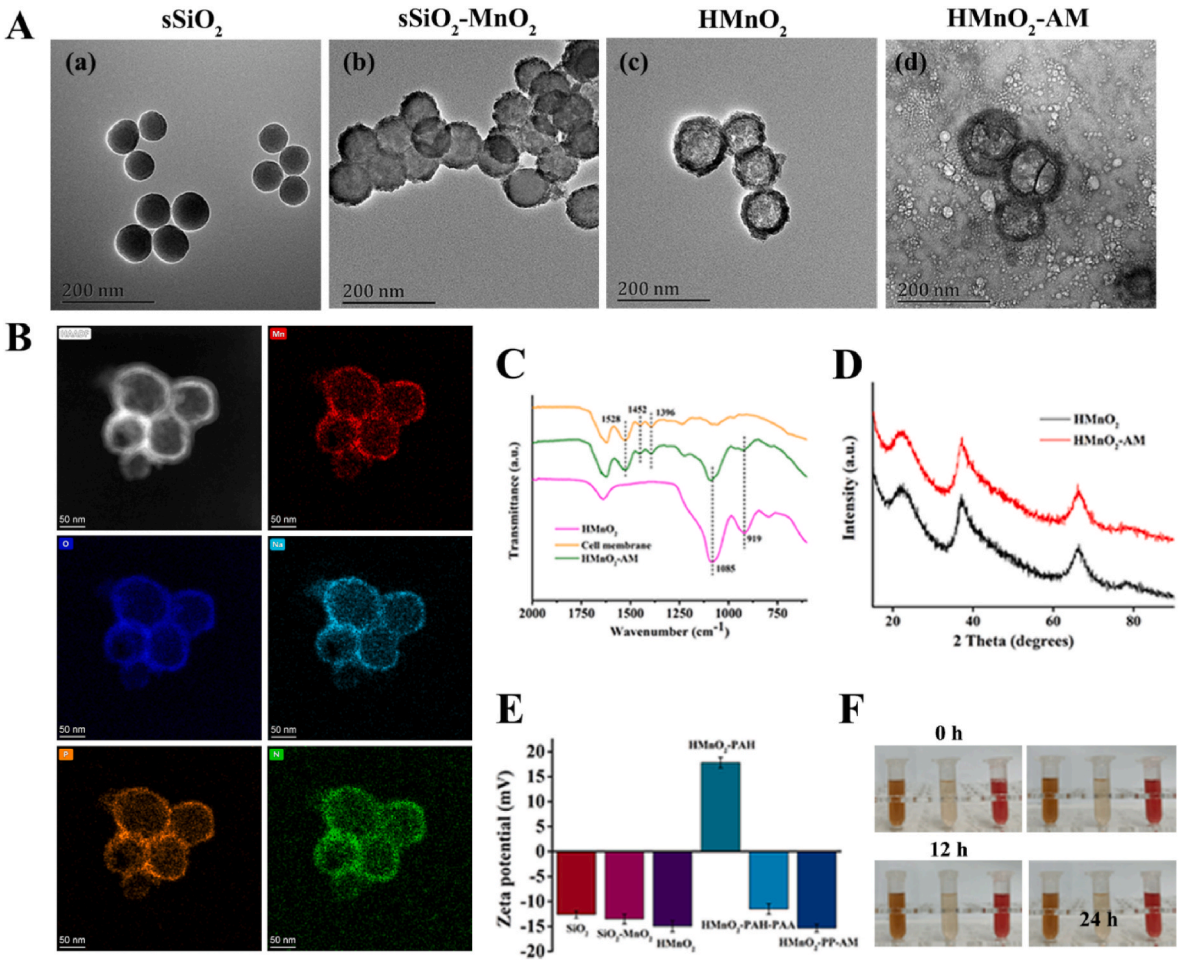

Fig. 1. (A) TEM images of (a) $sSiO_2$, (b) $sSiO_2$-MnO_2, (c) $HMnO_2$ and (d) $HMnO_2$-AM. (B) Elemental mapping of $HMnO_2$-AM nanoparticles, including bright field, Mn, O, Na, P and N. (C) FTIR spectra of $HMnO_2$, cell membrane and $HMnO_2$-AM. (D) XRD pattern of $HMnO_2$ and $HMnO_2$-AM. (E) Zeta potential of $sSiO_2$, $sSiO_2$-MnO_2, $HMnO_2$ and $HMnO_2$-AM. (F) The stability of Rh2@$HMnO_2$-AM in different solutions (FBS, H_2O and DMEM medium).

details, 1 mg Cy-5 was added to 10 mL of $HMnO_2$-AM suspension (50 μg/mL) and stirred for 12 h. After Cy-5@$HMnO_2$-AM was obtained, 100 μL of nanoparticles solution was intravenously injected into K7M2 tumor-bearing Balb/c nude mice through the tail vein. 24 h later, the mice were sacrificed and the major organs (heart, liver, spleen, lung, kidneys) were obtained for imaging via IVIS scanning for biodistribution.

To demonstrate the TME-triggered MRI contrast of Rh2@$HMnO_2$-AM nanoparticles for tumor-specific imaging, 100 μL ([Mn] = 50 μM) of Rh2@$HMnO_2$-AM solution was intravenously injected into the K7M2 tumor-bearing mice at predetermined time points (0, 4, 8, 12, 24 h) and mice were scanner via an MRI system. Subsequently, the *in vivo* tumors MRI images were collected at corresponding time points. The GSH-triggered off-to-on contrast enhancement enables Rh2@$HMnO_2$-AM nanoparticles become attractive for tumor MR imaging due to the fact that the GSH concentration in TME is approximately 1000 times higher than that in the extracellular matrix [52].

2.12. *In vivo antitumor efficacy and safety evaluation*

The orthotopic K7M2 tumor models were set up via the directly injection of K7M2 cells into the right leg of 25 Balb/c mice (4–6 weeks years old). The 25 mice were randomly divided into 5 groups (PBS, Rh2, $HMnO_2$, Rh2@$HMnO_2$, Rh2@$HMnO_2$-AM) when the tumor size grew to 30 mm^3 approximately. Subsequently, the PBS of control group or the suspension of nanoparticles (10 mg/kg) was injected gently from tail vein. During the observation period of tumor growth, tumor volume and body weight of mice were monitored and recorded every 3 days for 20 days. The tumor volume = $a \times b^2/2$, (a and b represents respectively the length and width of tumors). When the tumor volume rise went up about 1000 mm^3, the *in-situ* tumors were removed and their photographs were taken.

The excised tumor tissues were soaked in 4% paraformaldehyde, then embedded in paraffin and sectioned. The status of tumor tissue after different treatments was detected by TdT-mediated dUTP Nick-End Labeling (TUNEL) staining. The main organs of mice were removed and washed with PBS (to remove the extra blood), followed by soaking in formalin for the next-step H&E staining to further assess the *in vivo* toxicity of nanoparticles. Moreover, another 9 mice were treated with 100 μL of Rh2@$HMnO_2$-AM solution (10 mg/kg) on different time points (0, 3, 7 days), then the blood of mice was collected for the measurement of routine blood indicators, including red blood cell count (RBC), hematocrit (HCT), mean cell hemoglobin (MCH), platelet distributing width (PCT), hemoglobin concentration (HGB), red cell distribution width (RDW), mean cell volume (MCV), white blood cell count (WBC) and mean erythrocyte hemoglobin concentration (MCHC).

Serum samples were obtained from mice after a full course of treatment and diluted for measurement. Interleukin 6 (IL-6), interferon-γ (IFN-γ) and tumor necrosis factor α (TNF-α) were analyzed by the usage of ELISA kits.

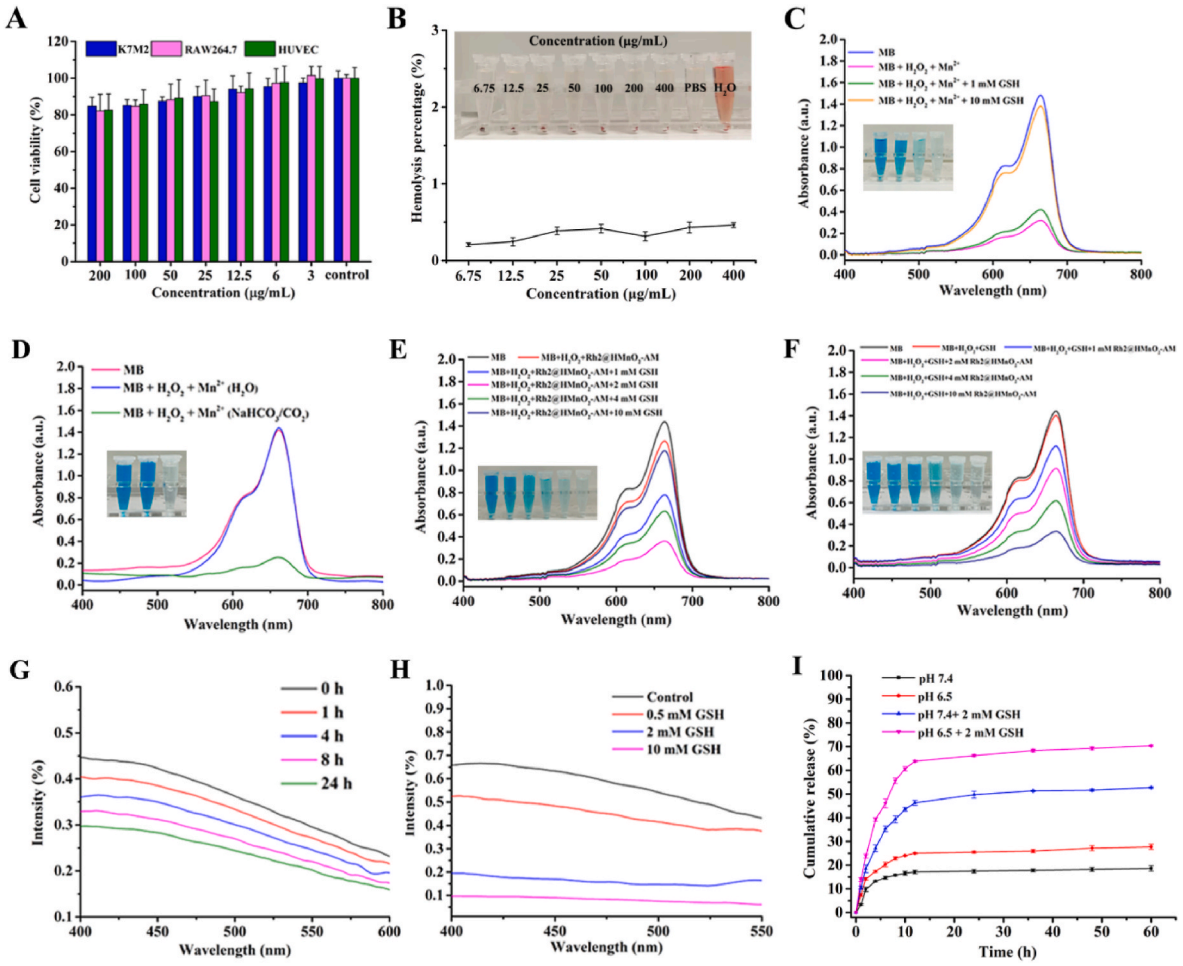

Fig. 2. (A) Cytotoxicity evaluation of HUVEC, K7M2 cell and RAW 264.7 with different concentrations of $HMnO_2$-AM nanoparticles for 24 h. (B) Hemolysis ratio and inset image of RBCs treated with various concentrations of $HMnO_2$-AM nanoparticles. (C) UV–vis absorption spectra and images (inset) of MB degradation via Mn^{2+}-triggered Fenton-like reaction with or without GSH (0, 1, 10 mM). (D) MB degradation via the Mn^{2+}-triggered Fenton-like process in different solutions with different solvent (H_2O or $NaHCO_3/CO_2$). (E) MB degradation by H_2O_2 plus GSH-treated Rh2@$HMnO_2$-AM nanoparticles. (F) MB degradation by 2 mM GSH plus different concentration of Rh2@$HMnO_2$-AM. UV–vis absorption spectra of $HMnO_2$-AM nanoparticles in (G) pH 6.5 for 1 h, 4 h, 8 h, and 12 h. (H) UV–vis absorption spectra of $HMnO_2$-AM nanoparticles in different concentration (0, 0.5, 2 and 10 mM) of GSH for 3 min at pH 7.4. (I) Drug releasing of Rh2@$HMnO_2$-AM nanoparticles in pH 7.4, pH 6.5, pH 7.4 + 2 mM GSH and pH 6.5 + 2 mM GSH.

2.13. *In vivo intratumorally distribution of immune cells*

The mice were euthanized and soaked in 80% alcohol for 3 min. The tumor tissue were obtained under sterile conditions, then extracted and stored in PBS solution, followed by the tumor sections were grinded in a sieve (200 mesh) to obtain a single cancer cell suspension. Subsequently, the lymphocytes suspension in the tumor sections was obtained via the usage of Tumor Infiltrating Lymphocyte Cell Separation Medium Kit. The prepared single cell suspension and an equal volume of the lymphocyte's separation solution were mixed and centrifuged with 500×*g* for 20 min under 25 °C. The second lymphocyte layer was collected and washed (using cell-washing solution). The tumor-infiltrating lymphocytes were centrifuged (300×*g*, 20 min) and collected. T cells were obtained by filtering lymphocytes through nylon wool column for 5 times. Further, the collected T cells were incubated with IgG isotype control, anti-CD3-PE, or anti-CD8-FITC antibodies to determine the $CD3^+$ and $CD8^+$ T cells in the tumors via the utilization of flow cytometry. The staining procedure of splenic T cells was similar to that of the tumor tissue and images were also obtained by confocal microscope.

2.14. *Immunofluorescence staining and biosafety*

The potential anti-tumor mechanism of the Rh2@$HMnO_2$-AM nanoparticles was explored via immunofluorescence due to the crucial roles of immune cells in tumor microenvironment. Tumor tissue sections were immersed in BSA solution (5%) at room temperature for 20 min after dewaxing, antigen regaining and permeabilization. Subsequently, sections were stained with mouse anti-CD4-PE, Alex 488-conjugated goat anti-mouse secondary antibody for marking $CD4^+$, and mouse anti-CD8-FITC, Rhodamine conjugated goat anti-rabbit secondary antibody for marking $CD8^+$, sections were stained at 4 °C overnight. DAPI was used to stain the nucleus. Images were obtained via a confocal microscope.

To evaluate the long-term organ toxicity of Rh2@$HMnO_2$-AM *in vivo*, 4–6 weeks of BALB/c nude mice were intravenously administered with Rh2@$HMnO_2$-AM (100 μg/mL, 100 μL). After one month, the mice were anesthetized, and the liver, lung, spleen, heart, and kidney were harvested, washed, fixed, sectioned, and hematoxylin and eosin (H&E) stained according to standard protocols for optical microscopic observation.

2.15. *Statistical analysis*

The obtained data are reported as mean ± standard deviation (SD). One-way analysis of variance (ANOVA) statistical method was performed to evaluate the experimental data. The criterion of statistical

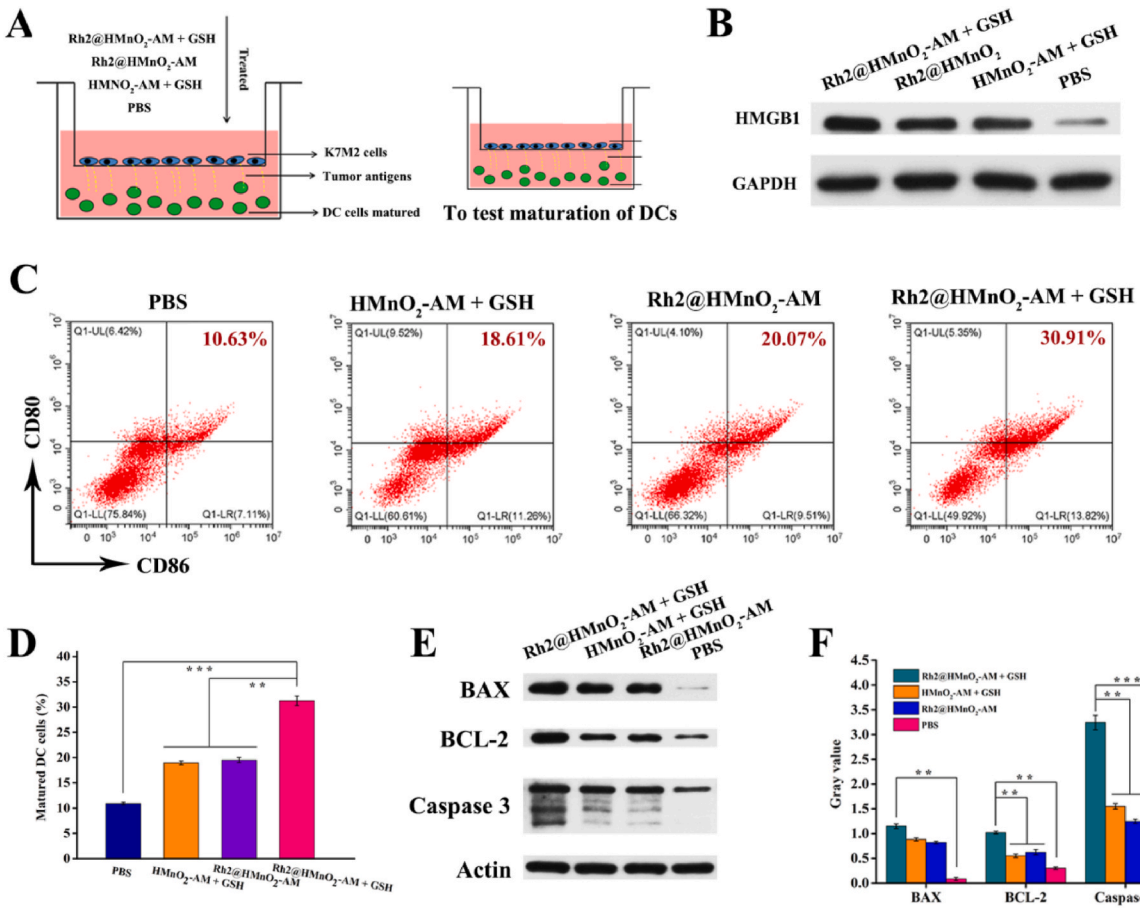

Fig. 3. (A) Scheme of K7M2 tumor cell co-culture system. K7M2 tumor cells were seeded in the upper chamber while DCs were cultured in lower chamber. (B) Western blot analysis of HMGB1 expression on K7M2 cells after different treatments. (C) Flow cytometric analysis and (D) quantification of DCs maturation after 24 h co-culture with K7M2 cells through treating with PBS, Rh2, $HMnO_2$-AM, Rh2@$HMnO_2$ or Rh2@$HMnO_2$-AM. (E) Western blot analysis and (F) quantification of BAX, BCL-2 and Caspase 3 of different groups.

significance for all tests were considered at $^*P < 0.05$, $^{**}P < 0.01$ and $^{***}P < 0.001$.

3. Results and discussion

3.1. Synthesis and characterization of Rh2@$HMnO_2$-AM

The procedure for the synthesis of Rh2@$HMnO_2$-AM is depicted in Scheme 1. Firstly, silica nanoparticles were used as a hard template for the generation of a uniform layer of MnO_2 by $KMnO_4$, followed by incubating the $sSiO_2$-MnO_2 complexed with Na_2CO_3 solution to obtain hollow MnO_2 nanoparticles ($HMnO_2$). The underlying mechanism of forming MnO_2 layer was supposed to be the fact that manganese permanganate ($KMnO_4$) could be reduced via unreacted organosilica existing on these freshly prepared $sSiO_2$. To modify $HMnO_2$ with alendronate, cationic polymer PAH and anionic polymer PAA were utilized as the "linker" through electrostatic interaction, followed by the amino-contained alendronate was conjugated to carboxyl-contained $HMnO_2$-PAH/PAA nanoparticles through amide formation for obtaining $HMnO_2$-PAH/PAA-ALD. Then, the K7M2 cells membrane was coated on the surface of $HMnO_2$-PAH/PAA-ALD to generate $HMnO_2$-AM nanoparticles. Lastly, traditional Chinese medicine ginsenosides Rh2 was loaded into $HMnO_2$-AM, yielding Rh2@$HMnO_2$-AM nanosystems (The "A" in $HMnO_2$-AM means alendronate and "M" means tumor cell membrane).

As Fig. 1A depicted, TEM images of $sSiO_2$, $sSiO_2$-MnO_2 and $HMnO_2$-AM nanoparticles clearly showed the spherical morphology and hollow structure with a diameter of approximately 141.5 nm. The element composition of $HMnO_2$-AM was determined to prove the presence of Mn, O, Na, P and N (Fig. 1B). Fourier transform infrared spectroscopy was used to confirm the $HMnO_2$-AM composition. As shown in Fig. 1C, the characteristic adsorption of $HMnO_2$ at 1085 cm^{-1} and 919 cm^{-1} and the characteristic peaks of cancer cell membranes at 1528 cm^{-1}, 1452 cm^{-1} and 1396 cm^{-1} were observed in $HMnO_2$-AM.

The X-ray diffraction (XRD) pattern of $HMnO_2$ (36.15°, 65.75°) and $HMnO_2$-AM (36.45°, 65.77°) had similar characteristic peaks and consistent with previous reports, which indicates that the surface modification of alendronate and cells membrane did not affect the crystal structure of $HMnO_2$ nanoparticles (Fig. 1D). The success of surface modification can be certified by zeta potential (Fig. 1E). The surface potential of nanoparticles changed from −12.63 eV to 17.78 eV after modification of PAH, then turning into −11.51 eV due to the carboxyl group of PAA and finally reaching at −15.32 eV after cell membrane coating. Moreover, the colloidal stability of Rh2@$HMnO_2$-AM was considered as a crucial indicator to assess their suitability for intravenous administration *in vivo*. The stability of the Rh2@$HMnO_2$-AM was observed in different media such as Fetal Bovine Serum (FBS), H_2O and DMEM medium. The digital photograph in Fig. 1F shows negligible aggregation or deposition in three solutions at various time points (0, 6, 12, 24 h), demonstrating excellent stability of Rh2@$HMnO_2$-AM.

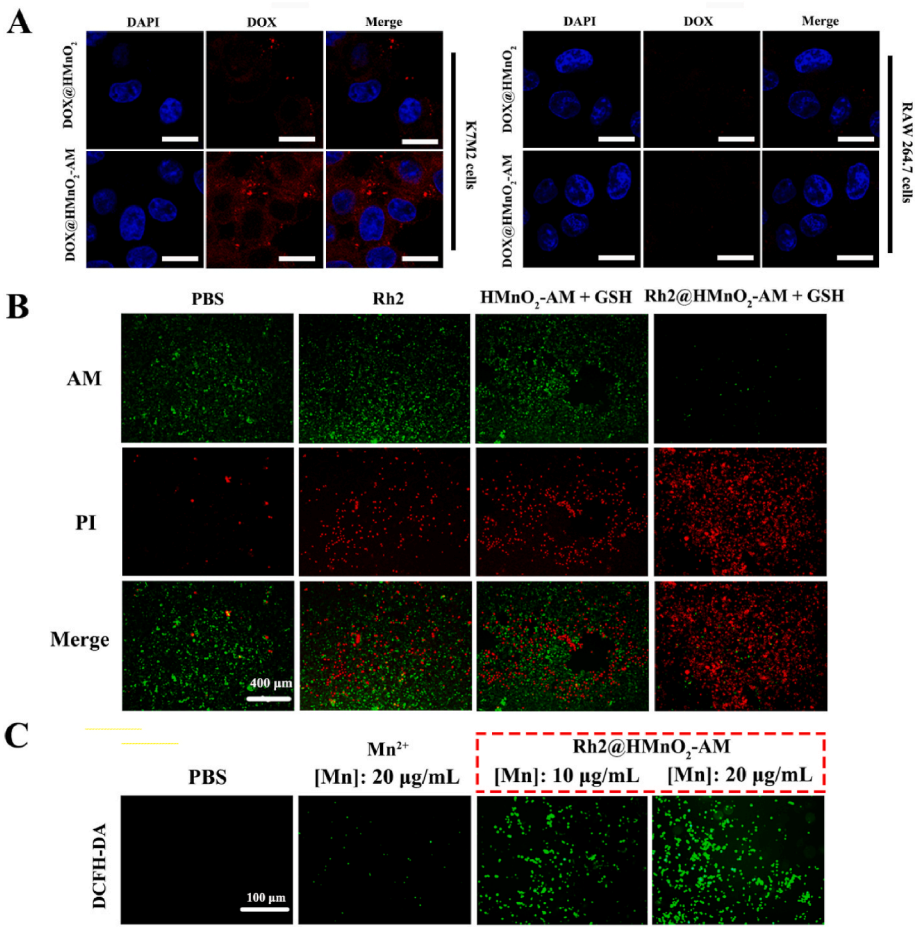

Fig. 4. (A) The CLSM images of K7M2 cells or RAW264.7 cells treated by DOX@$HMnO_2$ and DOX@$HMnO_2$-AM nanoparticles for 3 h (scale bar = 20 μm). (B) The Calcian-AM/PI staining of K7M2 cells after various treatments of PBS, $HMnO_2$-AM, Rh2, $HMnO_2$-AM + GSH and Rh2@$HMnO_2$ + GSH. The green fluorescence shows living cells and the red fluorescence represents dead cells. (C) DCFH-DA fluorescence of K7M2 cells exposed to $MnCl_2$ and Rh2@$HMnO_2$-AM with 2 mM GSH.

3.2. Cytotoxicity, drug release and in vitro chemodynamic activity of nanoparticles

To exert the therapeutic effects, we utilized CCK-8 assay to evaluate the cytotoxicity of $HMnO_2$-AM against three kinds of cells (K7M2, RAW 264.7 and HUVEC). It can be seen that the cell viability of $HMnO_2$-AM was still more than 80% when the concentration of nanoparticles was 200 μg/mL after 24 h incubation (Fig. 2A), which indicates $HMnO_2$-AM possess good cytocompatibility. Furthermore, the hemolysis ratio of RBCs was less than 1% even at 400 μg/mL of $HMnO_2$-AM, which ensures the blood safety of Rh2@$HMnO_2$ in clinical usage (Fig. 2B). The ·OH-generating activity of Fenton-like Mn^{2+} with the existence of HCO_3^- and the scavenging function of GSH on ·OH. We chose methylene blue (MB) as the indicator of ·OH formation. In Fig. 2C, the ·OH-triggered MB degradation was significantly inhibited with the existence of GSH, indicating that GSH can get rid of the generated ·OH and further restrict the CDT effect. As shown in Fig. 2D, a distinct decrease in absorbance was measured when MB was incubated with $MnCl_2$ and H_2O_2 for 30 min in $NaHCO_3/CO_2$ buffer. On the contrary, there is no apparent change in the MB absorbance was monitored after the same treatment in H_2O_2. As depicted in Fig. 2E, we evaluated the degradation rate of MB incubated with Rh2@$HMnO_2$-AM nanoparticles with GSH concentrations ranging from 1 to 10 mM. Obviously, the degradation rate of MB is highest when the GSH concentration was at 2 mM among various concentrations. Moreover, the degradation rate of MB increased (1–10 mM) with the increase of concentration of nanoparticles, reflecting the concentration-dependence of CDT (Fig. 2F). The Fenton-like reaction mentioned above is detailed as the following equations:

$$MnO_2 + GSH \rightarrow Mn^{2+} + GSSG \quad (1)$$

$$Mn^{2+} + H_2O_2 + HCO_3^- \rightarrow \cdot OH \quad (2)$$

The degradation of $HMnO_2$-AM triggered by GSH and acidic environment was detected by UV–vis absorption spectra. The absorption decreased over time at pH 6.5 (Fig. 2G) and the absorption decreased significantly at pH 7.4 after treatment with GSH (Fig. 2H). Furthermore, Rh2 release *in vitro* from Rh2@$HMnO_2$-AM nanoparticles was measured in PBS solution (pH 6.5, with or without 2 mM GSH) at 37 °C and PBS (pH 7.4, with or without equal amount of GSH). In Fig. 2I, Rh2@$HMnO_2$-AM nanoparticles exhibited pH-sensitive and GSH-sensitive Rh2 release. Rh2 was released slowly from Rh2@$HMnO_2$-AM nanoparticles both in pH 7.4 (about 15%) and pH 6.5 (about 22%) without GSH after 24 h. The minor differences may be attributed to the mild pH-sensitive degradation of $HMnO_2$ nanoparticles. However, a burst release occurred in reductive conditions after 12 h, and the highest Rh2 release reached more than 65% in pH 6.5 + 2 mM GSH and approximately 50% in pH 7.4 + 2 mM GSH. The results confirm that the Rh2@$HMnO_2$-AM nanoparticles could provide pH/redox dual responsiveness, which further supports the degradation property of $HMnO_2$-AM nanoparticles.

3.3. Activation of DC cells by Rh2@$HMnO_2$-AM and signaling pathway of in vitro therapy

To determine whether the ICD of K7M2 cells triggers the maturation

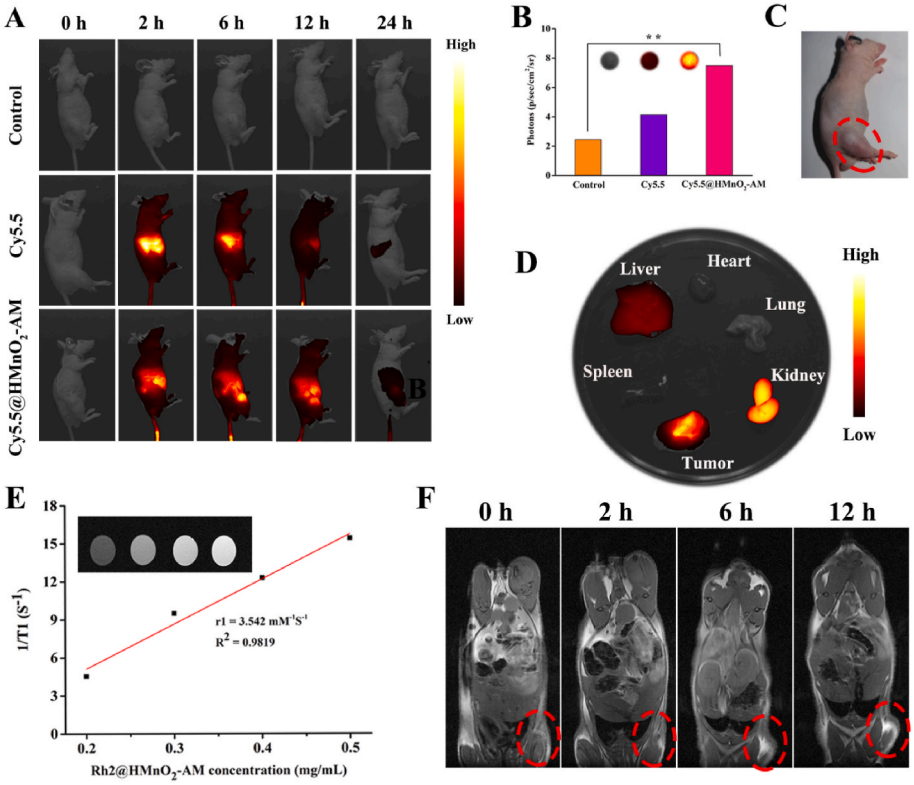

Fig. 5. *In vivo* imaging of Rh2@$HMnO_2$-AM nanoparticles in K7M2 tumor-bearing mice. (A) Fluorescence imaging of K7M2 tumor-bearing mice at pre-injection at different time points after injection of control, Cy5.5 and Cy5.5@$HMnO_2$-AM groups. (B) The statistical fluorescence intensity of tumors in different groups. (C) The image of K7M2-bearing mice (the red circle marks tumor site). (D) *Ex vivo* fluorescence imaging of main organs and tumor in Rh2@$HMnO_2$-AM group. (E) T1-weighted MR images of the Rh2@$HMnO_2$-AM. (F) T1-MR images of K7M2 tumor-bearing mice after injection of Rh2@$HMnO_2$-AM at different time points.

of DCs (a kind of immune cells that can regulate T-cell-triggered immune responses for killing the tumors), a transwell system was used to co-culture iDCs and K7M2 cells pretreated with different methods. The K7M2 cells in upper wells were treated with PBS, $HMnO_2$-AM, Rh2, Rh2@$HMnO_2$ or Rh2@$HMnO_2$-AM and iDCs were seeded in the bottom wells (Fig. 3A). After co-culture together overnight, DCs were measured via flow cytometry to assess the expression of CD80 and CD86 (the typical markers of DCs maturation) (Fig. 3B). It can been seen that K7M2 cells treated with Rh2@$HMnO_2$-AM obtained 30.91% of the DCs maturity, which was much higher than that of control (10.63%), single CDT (18.61%) and single immunotherapy (20.07%) groups (Fig. 3C). Furthermore, Fig. 3D showed that the ICD marker protein HMGB1 expression level reached highest in combined therapy group. The results revealed that immuno-chemodynamic synergistic therapy is significantly beneficial for ICD-based tumor immunotherapy through activating T cells.

To assess the immune response of immuno-chemodynamic combined therapy, we examined the characteristic markers (BAX, BCL-2 and Caspase 3 gene are all apoptosis-related gene) related to ICD in K7M2 cells after various treatments. As shown in Fig. 3E, the highest expression levels of BAX, BCL-2, and Caspase3 were observed in the Rh2@$HMnO_2$-AM + GSH group as compared to the control group, $HMnO_2$-AM + GSH and Rh2@$HMnO_2$-AM, which demonstrated treatments of Rh2@$HMnO_2$-AM + GSH can induce tumor cells apoptosis by the upregulation of BAX, BCL-2 and Caspase 3 level. In Fig. 3F, the gray values of BAX, BCL-2 and Caspase 3 were 1.15, 1.02 and 3.24 in Rh2@$HMnO_2$-AM + GSH, respectively, which higher than that in PBS group (0.086 of BAX, 0.3 of BCL-2 and 0.62 of Caspase 3).

3.4. Cellular uptake, ROS generation and in vitro therapy induced by Rh2@$HMnO_2$-AM

The intracellular uptake of Rh2@$HMnO_2$-AM nanoparticles was analyzed via CLSM. As depicted in Fig. 4A, there was significant red fluorescence in tumor cells treated with Rh2@$HMnO_2$-AM, which was stronger than that in RAW264.7 cells groups and in tumor cells treated with Rh2@$HMnO_2$. Subsequently, the *in vitro* CDT effect of Rh2@$HMnO_2$-AM was evaluated. In Fig. 4B, Rh2@$HMnO_2$-AM nanoparticles exhibited significantly greater anticancer efficiency, which could be attributed to the presence of Mn^{2+} and GSH depletion. As depicted in Fig. 4C and DCF fluorescence intensity in K7M2 cells exposed to Rh2@$HMnO_2$-AM nanoparticles were much higher than that in cells exposed to $MnCl_2$ at the same Mn concentration, showing that Rh2@$HMnO_2$-AM nanoparticles can cause more severe oxidative stress in K7M2 cells, which provides strong support for the excellent therapeutic functionality of Rh2@$HMnO_2$-AM nanoparticles as compared to Mn^{2+}.

3.5. In vitro and in vivo imaging of Rh2@$HMnO_2$-AM nanoparticles

After demonstrating the immuno-chemodynamic combination osteosarcoma therapy effect of Rh2@$HMnO_2$-AM *in vitro* experiments, the mouse *in-situ* K7M2 tumor model was established to further assess therapeutic potential. We tracked Rh2@$HMnO_2$-AM *in vivo* via intravenous (i.v.) injection of Cy5.5-labeled $HMnO_2$-AM (Cy5.5@ $HMnO_2$-AM, 10 mg/kg) (Fig. 5A–D). The Cy5.5 fluorescence signals in the tumor region enhanced and reached a peak level at 8 h post injection, revealing the efficient tumor accumulation of Rh2@$HMnO_2$-AM. Moreover, strong fluorescence of Cy5.5 observed in kidneys of mice after injection of Cy5.5@$HMnO_2$-AM illustrated rapid renal clearance of Cy5.5 after decomposition of nanoparticles.

In order to examine the MRI contrast effect of Rh2@$HMnO_2$-AM, *in vitro* and *in vivo* MRI imaging effects were detected. To confirm this, various concentrations (0.2, 0.3, 0.4 and 0.5 mg/mL) of Rh2@$HMnO_2$-AM nanoparticles were used to assess their *in vitro* MR imaging capability. As shown in Fig. 5E, the MRI signal was enhanced with the increasing of Rh2@$HMnO_2$-AM concentration. Then, the *in vivo* MRI imaging capability of Rh2@$HMnO_2$-AM was performed on K7M2 tumor-bearing mice (Fig. 5F). Obviously, the tumor area showed significantly enhanced T1-MR contrast after injection of Rh2@$HMnO_2$-AM with

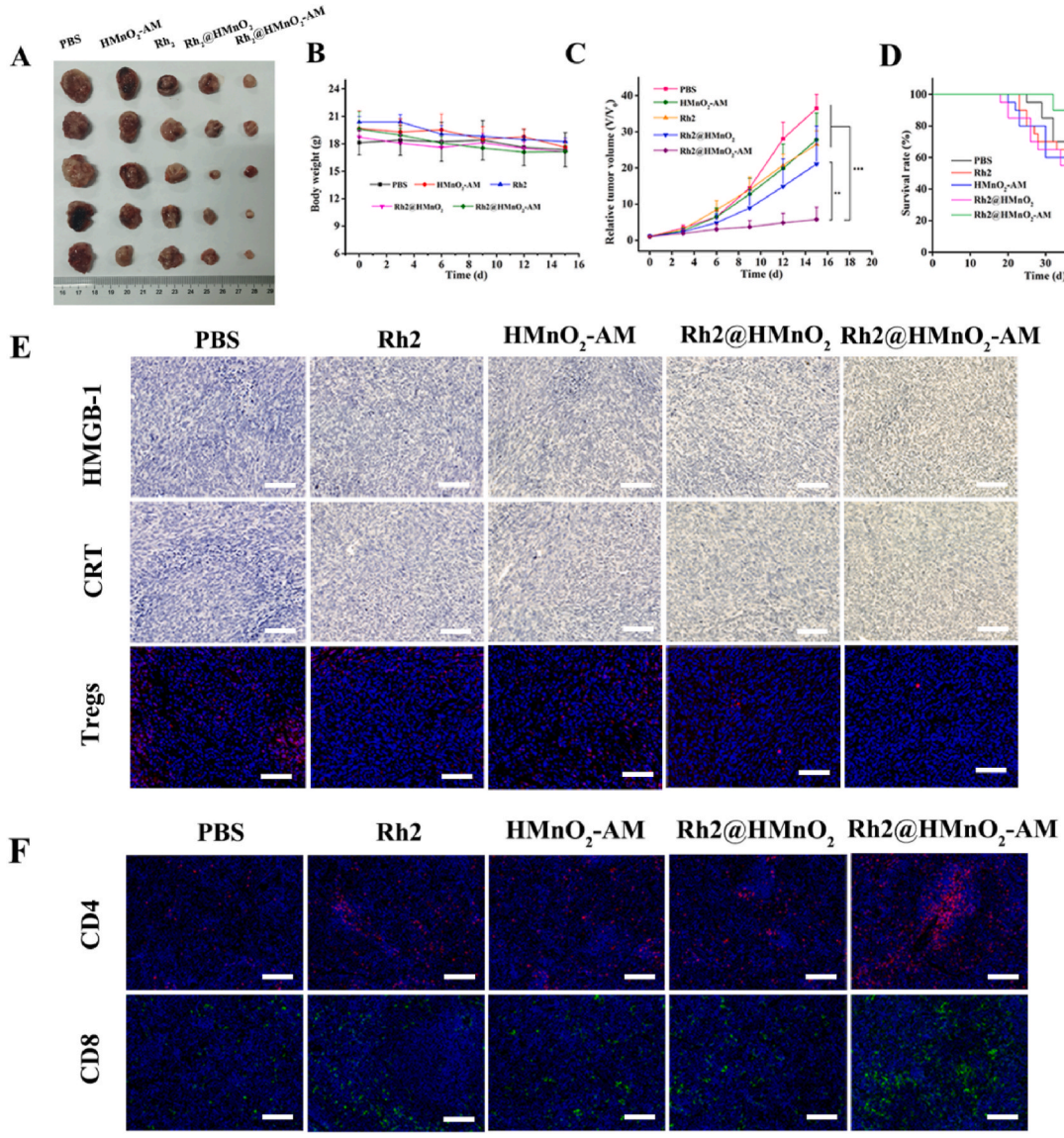

Fig. 6. (A) Tumor photos of mice in 15 days of different groups. (B) The body weight of K7M2 tumor-bearing mice at different time points. (C) Relative tumor volume of mice after various treatments. (D) Survival curves of K7M2-tumor bearing mice after different treatments. (E) Immunohistochemical analysis of HMGB-1 and CRT, and immunofluorescence staining of Tregs in tumor tissue. (F) Representative immunofluorescence staining of $CD4^+$ (red) and $CD8^+$ (green) T cells in spleen. Scale bar represents 100 μm for each panel. (For interpretation of the references to color in this figure legend, the reader is referred to the Web version of this article.)

passage of time and signals peaked at 6 h, which is consistent with the results of fluorescence imaging. This phenomenon provides the direct evidence that Rh2@$HMnO_2$-AM has good affinity to K7M2 tumor tissue.

3.6. *Rh2@$HMnO_2$-AM nanoparticles inhibited tumor growth and enhanced infiltration of immune cells into tumor and spleen*

Based on the experiment results *in vitro*, the *in-situ* tumor model was established to measure the effects of combined CDT and immunotherapy *in vivo*. In Figs. 6A and S3, Rh2@$HMnO_2$-AM exhibited the excellent inhibition effect on tumor growth. Body weight was measured during the course of treatment to investigate whether the Rh2@$HMnO_2$-AM had any systemic toxicity. As shown in Fig. 6B, differences in body weight were negligible in treated mice as compared to control groups. In Fig. 6C, the relative tumor volume of Rh2@$HMnO_2$-AM group only about 5.7 compared to 21.07 in Rh2@$HMnO_2$, 27.76 in $HMnO_2$-AM group, and 36.45 in PBS group, indicating that Rh2@$HMnO_2$-AM had a remarkable osteosarcoma inhibition. Moreover, the mice survival rate was assessed by dividing 50 mice into 5 groups. The Rh2@$HMnO_2$-AM group kept survival for over 55 d, while other groups showed a relatively short average life span (Fig. 6D). Moreover, the stronger green fluorescence in TUNEL staining showed that Rh2@$HMnO_2$-AM caused more cancer cell death (Fig. S1). The weaker red fluorescence indicated that Rh2@$HMnO_2$-AM significantly alleviated hypoxia within tumors (Fig. S2). Taken together, the results revealed an excellent combined therapy efficacy of Rh2@$HMnO_2$-AM nanoparticles.

Here, the immunohistochemical staining was conducted to assess the ICD markers (such as HMGB-1 and CRT) expression in tumors after various treatments. When compared to PBS group, the treatment with Rh2@$HMnO_2$-AM induces a significant HMGB-1, and consistent results can be observed for the CRT expression (Fig. 6E), suggesting that the enhanced tumor antigen presentation could trigger DCs maturation to some extent. Tumor-infiltrating $FOXP3^+$ T cells (Tregs) reflect immune escape in tumor microenvironment, and the decrease of Tregs population plays an important role in realizing effective tumor immunotherapy. The population of Tregs was measured through immunofluorescence staining of Foxp3 protein (a typical marker of Tregs). The Foxp3 protein level in Rh2@$HMnO_2$-AM group was

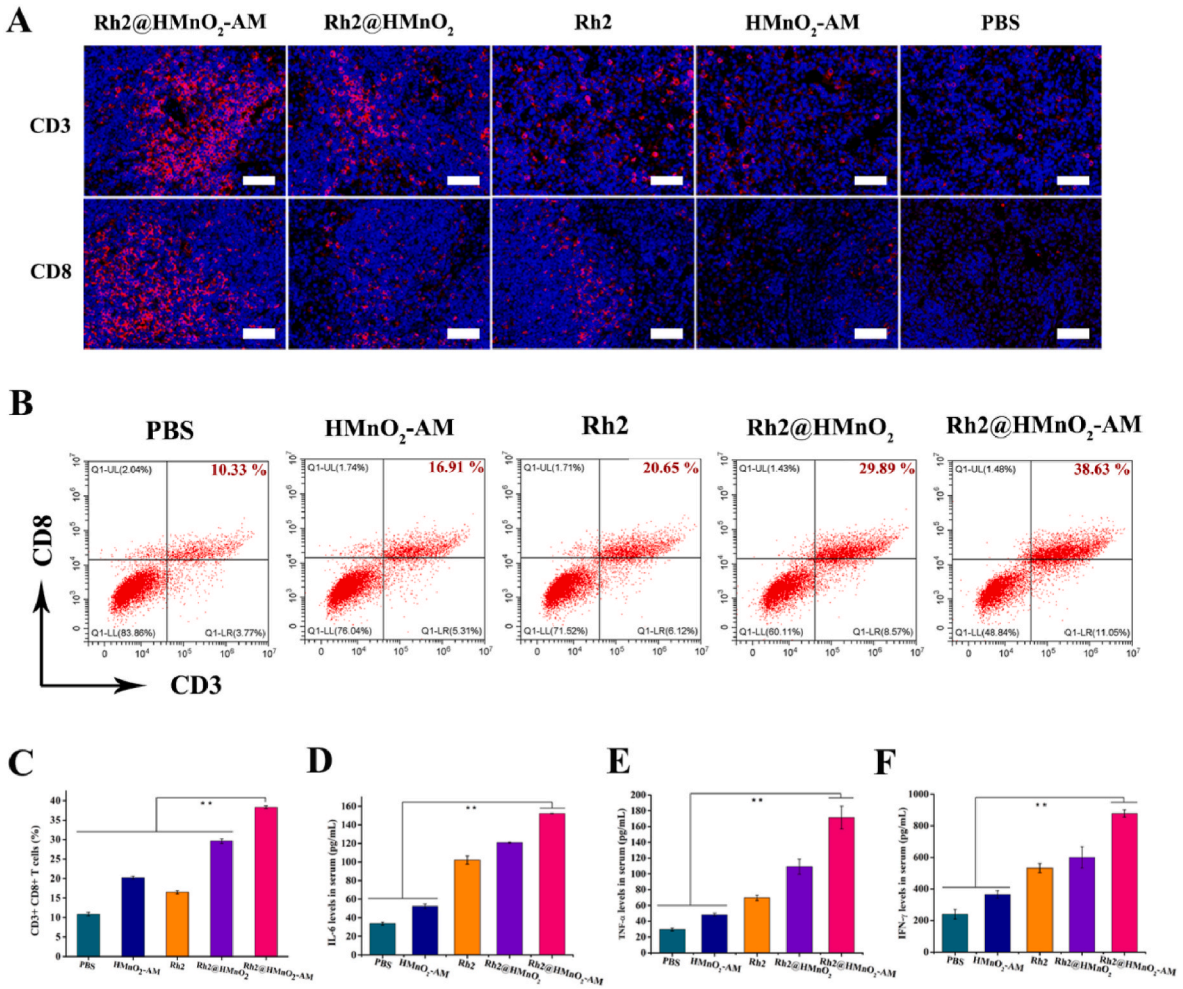

Fig. 7. (A) Representative immunofluorescence staining of $CD3^+$ and $CD8^+$ T cells in tumor tissue. (B) Flow cytometric examination and (C) quantitative analysis of intratumor infiltration of $CD3^+$ and $CD8^+$ T cells. Contents of the (D) IL-6, (E) TNF-α and (F) IFN-γ in serum of mice on the 14th day after treatment with PBS, Rh2, $HMnO_2$-AM, Rh2@$HMnO_2$ or Rh2@$HMnO_2$-AM. Scale bar represents 100 μm for each panel.

obviously lower than other groups, which proves the mechanism of tumor immunotherapy with Tregs reduction and demonstrates the feasibility of Rh2@$HMnO_2$-AM-mediated tumor immunotherapy (Fig. 6E).

To assess the possible ICD-induced activation of T cells after the immuno-chemodynamic combined therapy, the distribution of adaptive T cells in the spleens was inspected via immunofluorescence staining (Fig. 6F). In spleen region, the $CD4^+$ (red fluorescence) and $CD8^+$ (green fluorescence) T cells in Rh2@$HMnO_2$-AM group have the largest distribution among all groups.

To assess the activation of T cells after the combined therapy, the distribution of T cells in tumors was measured via immunofluorescence staining of tumor tissues (Fig. 7A). Apparently, the $CD3^+$ and $CD8^+$ T cells in Rh2@$HMnO_2$-AM group have the largest distribution among all treatments, followed by the Rh2@$HMnO_2$, Rh2, $HMnO_2$-AM, and PBS groups. To analyze the phenotype of tumor T cells by flow cytometry, we extracted the T cells and examined the purity of the cells linked to the fluorescein isothiocyanate-labeled CD3 and CD8 antibody by flow cytometry (Fig. 7B and C). The populations of $CD3^+/CD8^+$ T cells after different treatments follow the order of Rh2@$HMnO_2$-AM (38.63%) > Rh2@$HMnO_2$ (29.89%) > Rh2 (20.65%) > $HMnO_2$-AM (16.91%) > PBS (10.33%).

To investigate the effective T cell-related cancer immunotherapy, the level of IL-6, TNF-α and IFN-γ in the serum of mice after different treatments were determined using the corresponding ELISA assay (Fig. 7D–F). Obviously, the level of IL-6, TNF-α and IFN-γ in Rh2@$HMnO_2$-AM group were in an order of Rh2@$HMnO_2$-AM > Rh2@$HMnO_2$ > Rh2 > $HMnO_2$-AM > PBS. The highest expression of those cytokines on Rh2@$HMnO_2$-AM group further indicates the cooperative enhancement of tumor inhibition via MRI-guided immuno-chemodynamic combination therapy to result in the best T cell-mediated antitumor immune responses.

3.7. *Biosafety in vivo of Rh2@$HMnO_2$-AM nanoparticles*

Moreover, in order to assess the biosafety of Rh2@$HMnO_2$-AM, the level of white blood cell (WBC) counts, red blood cell (RBC) counts, hematocrit (HCT), mean corpuscular hemoglobin (MCH), mean corpuscular volume (MCV), mean corpuscular hemoglobin concentration (MCHC), Red Cell volume Distribution width (RDW), hemoglobin (HGB), and platelets (PLT) were tested and there was no significant difference in the content at 0, 3 and 7 days (Fig. S4). Subsequently, the H&E staining images of major organs demonstrated no necrosis of the cells damage after the injection of Rh2@$HMnO_2$-AM for 7 days, which further exhibited negligible toxicity and excellent biocompatibility of Rh2@$HMnO_2$-AM (Fig. S5).

4. Conclusions

In summary, we designed a kind of herbal medicine-loaded

biodegradable nanosparticles with bone-targeting and tumor-homing capability for MRI-guided immuno-chemodynamic combination osteosarcoma therapy. ALD/K7M2 cell membranes-coated $HMnO_2$ is considered ideal TME-activated nanoparticles due to its well-established preparation method, higher loading, better biosafety, and long cycling properties *in vivo*. Rh2, the Chinese herbal medicine, is released within the tumor, triggering the ICD, further leading to infiltration and activation of T cells, inducing the upregulation of BAX and BCL-2, and promoting the secretion of IL-6, TNF-α and IFN-γ. Meanwhile, ·OH produced from Mn^{2+}-mediated CDT can acutely promote the apoptosis of tumor cells and further benefit antitumor immunity. This multifunctional theranostic nanoparticles exhibits excellent target function towards osteosarcoma, TME-activated MRI imaging capability and Rh2 release which enhance the ability of innate immunity inside the tumor. Overall, this study demonstrates the potential of Rh2@$HMnO_2$-AM nanoparticles for simultaneous MRI imaging and effective treatment of osteosarcoma, providing an appealing strategy for imaging-guided cancer therapy and further clinical translation.

CRediT authorship contribution statement

Liwen Fu: ConceptualizationConceptualizaiton, Investigation, Data curation, Writing – original draft. **Weiying Zhang:** Methodology, Visualization. **Xiaojun Zhou:** Supervision, Writing - review & editing. **Jingzhong Fu:** Supervision, Methodology. **Chuanglong He:** Supervision, Funding acquisition, Writing - review & editing.

Declaration of competing interest

The authors declare that they have no known competing financial interests or personal relationships that could have appeared to influence the work reported in this paper.

Acknowledgments

This work was financially supported by the National Natural Science Foundation of China (31771048, 32071350), Fundamental Research Funds for the Central Universities (2232018A3-07, 2232019A3-06), International Cooperation Fund of the Science and Technology Commission of Shanghai Municipality (19440741600).

Appendix A. Supplementary data

Supplementary data to this article can be found online at https://doi.org/10.1016/j.bioactmat.2022.01.035.

References

[1] Q. Hu, C. Qian, W. Sun, J. Wang, Z. Chen, H.N. Bomba, H. Xin, Q. Shen, Z. Gu, Engineered nanoplatelets for enhanced treatment of multiple myeloma and thrombus, Adv. Mater. 28 (43) (2016) 9573–9580.
[2] F. Macedo, K. Ladeira, F. Pinho, N. Saraiva, N. Bonito, L. Pinto, F. Goncalves, Bone metastases: an overview, Onco Rev. 11 (1) (2017), 321-321.
[3] R.K. Heck Jr., M.A. Peabody Td Fau - Simon, M.A. Simon, Staging of primary malignancies of bone, Ca-Cancer, J. Clin. 56 (6) (2006) 366–375.
[4] M. Kovac, C. Blattmann, S. Ribi, J. Smida, N.S. Mueller, F. Engert, F.A.-O. Castro-Giner, J. Weischenfeldt, M. Kovacova, A. Krieg, D.A.-O. Andreou, P.U. Tunn, H. R. Dürr, H. Rechl, K.D. Schaser, I. Melcher, S. Burdach, A. Kulozik, K. Specht, K. Heinimann, S. Fulda, S. Bielack, G. Jundt, I. Tomlinson, J.A.-O. Korbel, M. Nathrath, D. Baumhoer, Exome sequencing of osteosarcoma reveals mutation signatures reminiscent of BRCA deficiency, Nat. Commun. 6 (2015) 8940.
[5] A. Schroeder, M. M. Heller Da Fau - Winslow, J. E. Winslow Mm Fau - Dahlman, G. W. Dahlman Je Fau - Pratt, R. Pratt Gw Fau - Langer, T. Langer R Fau - Jacks, D. G. Jacks T Fau - Anderson and D. G. Anderson, Treating metastatic cancer with nanotechnology, Nat. Rev. Cancer 12 (1) 39-50.
[6] R. Vinay and V. KusumDevi, Potential of targeted drug delivery system for the treatment of bone metastasis, Drug Deliv.. 23 (1) 2016 21-29.
[7] F. Duffaud, O. Mir, P. Boudou-Rouquette, S. Piperno-Neumann, N. Penel, E. Bompas, C. Delcambre, E. Kalbacher, A. Italiano, O. Collard, C. Chevreau, E. Saada, N. Isambert, J. Delaye, C. Schiffler, C. Bouvier, V. Vidal, S. Chabaud, J.-Y. Blay, Efficacy and safety of regorafenib in adult patients with metastatic osteosarcoma: a non-comparative, randomised, double-blind, placebo-controlled, phase 2 study, Lancet Oncol. 20 (1) (2019) 120–133.
[8] S. Behjati, P.S. Tarpey, K. Haase, H. Ye, M.D. Young, L.B. Alexandrov, S.J. Farndon, G. Collord, D.C. Wedge, I. Martincorena, S.L. Cooke, H. Davies, W. Mifsud, M. Lidgren, S. Martin, C. Latimer, M. Maddison, A.P. Butler, J.W. Teague, N. Pillay, A. Shlien, U. McDermott, P.A. Futreal, D. Baumhoer, O. Zaikova, B. Bjerkehagen, O. Myklebost, M.F. Amary, R. Tirabosco, P. Van Loo, M.R. Stratton, A.M. Flanagan, P.J. Campbell, Recurrent mutation of IGF signalling genes and distinct patterns of genomic rearrangement in osteosarcoma, Nat. Commun. 8 (1) (2017) 15936.
[9] L. Fu, X. Zhou, C.A.-O. He, Polymeric nanosystems for immunogenic cell death-based cancer immunotherapy, Macromol. Biosci. 21 (7) (2021), e2100075.
[10] H. Ledford, Therapeutic cancer vaccine survives biotech bust, Nature 519 (7541) (2015) 17–18.
[11] S. Fu, R. Yang, J. Ren, J. Liu, L. Zhang, Z.A.-O. Xu, Y.A.-O. Kang, P.A.-O. Xue, Catalytically active $CoFe_2O_4$ nanoflowers for augmented sonodynamic and chemodynamic combination therapy with elicitation of robust immune response, ACS Nano 15 (7) (2021) 11953–11969.
[12] W. Hu, T. Xiao, D. Li, Y. Fan, L. Xing, X. Wang, Y. Li, X.A.-O. Shi, M.A.-O. Shen, Intelligent molybdenum disulfide complexes as a platform for cooperative imaging-guided tri-mode chemo-photothermo-immunotherapy, Adv. Sci. 8 (14) (2021) 2100165.
[13] J. Han, Y. Kwon, D.-C. Yang, Y. Jung, Y.E. Choi, Expression and RNA interference-induced silencing of the dammarenediol synthase gene in panax ginseng, Plant Cell Physiol. 47 (2007) 1653–1662.
[14] H.-S. Kim, E.-H. Lee, S.-R. Ko, K.-J. Choi, J.-H. Park, D.-S. Im, Effects of ginsenosides Rg3 and Rh2 on the proliferation of prostate cancer cells, Arch Pharm. Res. (Seoul) 27 (4) (2004) 429.
[15] J. Liu, Q. Cai, W. Wang, M. Lu, J. Liu, F. Zhou, M. Sun, G. Wang, J. Zhang, Ginsenoside Rh2 pretreatment and withdrawal reactivated the pentose phosphate pathway to ameliorate intracellular redox disturbance and promoted intratumoral penetration of adriamycin, Redox Biol. 32 (2020) 101452.
[16] B. Li, J. Zhao, C.-Z. Wang, J. Searle, T.-C. He, C.-S. Yuan, W. Du, Ginsenoside Rh2 induces apoptosis and paraptosis-like cell death in colorectal cancer cells through activation of p53, Cancer Lett. 301 (2) (2011) 185–192.
[17] H. Hasegawa, J.-H. Sung, S. Matsumiya, M. Uchiyama, Main ginseng saponin metabolites formed by intestinal bacteria, Planta Med. 62 (5) (1996) 453–457.
[18] J. Zhang, J. Zhou, Q. Yuan, C. Zhan, Z. Shang, Q. Gu, J. Zhang, G. Fu and W. Hu, Characterization of ginsenoside compound K loaded ionically cross-linked carboxymethyl chitosan-calcium nanoparticles and its cytotoxic potential against prostate cancer cells, J. Cinseng Res. 45 (2) 228-235.
[19] P. Li, X. Zhou, D. Qu, M. Guo, C. Fan, T. Zhou, Y. Ling, Preliminary study on fabrication, characterization and synergistic anti-lung cancer effects of self-assembled micelles of covalently conjugated celastrol-polyethylene glycol-ginsenoside Rh2, Drug Deliv. 24 (1) (2017) 834–845.
[20] T.G. Liu, D.-D. Huang Y Fau - Cui, X.-B. Cui Dd Fau - Huang, S.-H. Huang Xb Fau - Mao, L.-L. Mao Sh Fau - Ji, H.-B. Ji Ll Fau - Song, C. Song Hb Fau - Yi, C. Yi, Inhibitory effect of ginsenoside Rg3 combined with gemcitabine on angiogenesis and growth of lung cancer in mice, BMC Cancer 9 (2009) 250.
[21] C. Zhang, W. Bu, D. Ni, S. Zhang, Q. Li, Z. Yao, J. Zhang, H. Yao, Z. Wang, J. Shi, Synthesis of iron nanometallic glasses and their application in cancer therapy by a localized Fenton reaction, Angew. Chem. Int. Ed. 55 (6) (2016) 2101–2106.
[22] Z. Tang, Y. Liu, M. He, W.A.-O. Bu, Chemodynamic therapy: tumour microenvironment-mediated Fenton and fenton-like reactions, Angew. Chem. Int. Ed. 58 (4) (2019) 946–956.
[23] W.Y. Pan, K.J. Lin, C.C. Huang, W.L. Chiang, Y.J. Lin, W.C. Lin, E.Y. Chuang, Y. Chang, H.W. Sung, Localized sequence-specific release of a chemopreventive agent and an anticancer drug in a time-controllable manner to enhance therapeutic efficacy, Biomaterials 101 (2016) 241–250.
[24] M. F. Chung, H. Y. Liu, K. J. Lin, W. T. Chia and H. W. Sung, A pH-responsive carrier system that generates NO bubbles to trigger drug release and reverse P-Glycoprotein-Mediated multidrug resistance, Angew. Chem. Int. Ed. 54 (34) 9890-9893.
[25] T. He, C. Jiang, J. He, Y. Zhang, G. He, J. Wu, J. Lin, X. Zhou, P. Huang, Manganese-dioxide-coating-instructed plasmonic modulation of gold nanorods for activatable duplex-imaging-guided NIR-II photothermal-chemodynamic therapy, Adv. Mater. 33 (13) (2021) 2008540.
[26] K.H. Min, H.J. Min Hs Fau - Lee, D.J. Lee Hj Fau - Park, J.Y. Park Dj Fau - Yhee, K. Yhee Jy Fau - Kim, I.C. Kim K Fau - Kwon, S.Y. Kwon Ic Fau - Jeong, O.F. Jeong Sy Fau - Silvestre, X. Silvestre Of Fau - Chen, Y.-S. Chen X Fau - Hwang, E.-C. Hwang Ys Fau - Kim, S.C. Kim Ec Fau - Lee, S.C. Lee, pH-controlled gas-generating mineralized nanoparticles: a theranostic agent for ultrasound imaging and therapy of cancers, ACS Nano 9 (1) (2015) 134–145.
[27] Z. Liu, X. Chen, Simple bioconjugate chemistry serves great clinical advances: albumin as a versatile platform for diagnosis and precision therapy, Chem. Soc. Rev. 45 (5) (2016) 1432–1456.
[28] G. Yang, L. Xu, Y. Chao, J. Xu, X. Sun, Y. Wu, R. Peng, Z. Liu, Hollow MnO_2 as a tumor-microenvironment-responsive biodegradable nano-platform for combination therapy favoring antitumor immune responses, Nat. Commun. 8 (1) (2017) 902.
[29] W. Zhu, Z. Dong, T. Fu, J. Liu, Q. Chen, Y. Li, R. Zhu, L. Xu, Z. Liu, Modulation of hypoxia in solid tumor microenvironment with MnO2 nanoparticles to enhance photodynamic therapy, Adv. Funct. Mater. 26 (30) (2016) 5490–5498.
[30] H. Lin, Y. Chen, J. Shi, Nanoparticle-triggered in situ catalytic chemical reactions for tumour-specific therapy, Chem. Soc. Rev. 47 (6) (2018) 1938–1958.
[31] L.-S. Lin, J. Song, L. Song, K. Ke, Y. Liu, Z. Zhou, Z. Shen, J. Li, Z. Yang, W. Tang, G. Niu, H.-H. Yang, X. Chen, Simultaneous fenton-like ion delivery and glutathione

depletion by MnO2-based nanoagent to enhance chemodynamic therapy, Angew. Chem. Int. Ed. 57 (18) (2018) 4902–4906.
[32] X. Cai, W. Gao, M. Ma, M. Wu, L. Zhang, Y. Zheng, H. Chen, J. Shi, A prussian blue-based core–shell hollow-structured mesoporous nanoparticle as a smart theranostic agent with ultrahigh pH-responsive longitudinal relaxivity, Adv. Mater. 27 (41) (2015) 6382–6389.
[33] Y. Chen, Q. Yin, X. Ji, S. Zhang, H. Chen, Y. Zheng, Y. Sun, H. Qu, Z. Wang, Y. Li, X. Wang, K. Zhang, L. Zhang, J. Shi, Manganese oxide-based multifunctionalized mesoporous silica nanoparticles for pH-responsive MRI, ultrasonography and circumvention of MDR in cancer cells, Biomaterials 33 (29) (2012) 7126–7137.
[34] R. Wei, X. Gong, H. Lin, K. Zhang, A. Li, K. Liu, H. Shan, X. Chen, J. Gao, Versatile octapod-shaped hollow porous manganese(II) oxide nanoplatform for real-time visualization of cargo delivery, Nano Lett. 19 (8) (2019) 5394–5402.
[35] P. Prasad, C.R. Gordijo, A.Z. Abbasi, A. Maeda, A. Ip, A.M. Rauth, R.S. DaCosta, X. Y. Wu, Multifunctional albumin–MnO_2 nanoparticles modulate solid tumor microenvironment by attenuating hypoxia, acidosis, vascular endothelial growth factor and enhance radiation response, ACS Nano 8 (4) (2014) 3202–3212.
[36] A.Z. Abbasi, P. Prasad, P. Cai, C. He, W.D. Foltz, M.A. Amini, C.R. Gordijo, A. M. Rauth, X.Y. Wu, Manganese oxide and docetaxel co-loaded fluorescent polymer nanoparticles for dual modal imaging and chemotherapy of breast cancer, J. Contr. Release 209 (2015) 186–196.
[37] Z. Zeng, K. Pu, Improving cancer immunotherapy by cell membrane-camouflaged nanoparticles, Adv. Funct. Mater. 30 (43) (2020) 2004397.
[38] Z. Chen, P. Zhao, Z. Luo, M. Zheng, H. Tian, P. Gong, G. Gao, H. Pan, L. Liu, A. Ma, H. Cui, Y. Ma, L. Cai, Cancer cell membrane–biomimetic nanoparticles for homologous-targeting dual-modal imaging and photothermal therapy, ACS Nano 10 (11) (2016) 10049–10057.
[39] J. Shen, J. Karges, K. Xiong, Y. Chen, L. Ji, H. Chao, Cancer cell membrane camouflaged iridium complexes functionalized black-titanium nanoparticles for hierarchical-targeted synergistic NIR-II photothermal and sonodynamic therapy, Biomaterials 275 (2021) 120979.
[40] C. Chen, M. Song, Y. Du, Y. Yu, C. Li, Y. Han, F. Yan, Z. Shi, S. Feng, Tumor-associated-macrophage-membrane-coated nanoparticles for improved photodynamic immunotherapy, Nano Lett. 21 (13) (2021) 5522–5531.
[41] R.H. Fang, C.-M.J. Hu, B.T. Luk, W. Gao, J.A. Copp, Y. Tai, D.E. O'Connor, L. Zhang, Cancer cell membrane-coated nanoparticles for anticancer vaccination and drug delivery, Nano Lett. 14 (4) (2014) 2181–2188.
[42] Y.Y. Fan, Y. Cui, W.Y. Hao, M.Y. Chen, Q.Q. Liu, Y.L. Wang, M.Y. Yang, Z.P. Li, W. Gong, S.Y. Song, Y. Yang, C.S. Gao, Carrier-free highly drug-loaded biomimetic nanosuspensions encapsulated by cancer cell membrane based on homology and active targeting for the treatment of glima, Bioact. Mater. 6 (12) (2021) 4402–4414.
[43] T. Zhang, H. Liu, L. Li, Z.Y. Guo, J. Song, X.Y. Yang, G.Y. Wan, R.S. Li, Y.S. Wang, Leukocyte/platelet hybrid membrane-camouflaged dendritic large pore mesoporous silica nanoparticles co-loaded with photo/chemotherapeutic agents for triple negative breast cancer combination treatment, Bioact. Mater. 6 (11) (2021) 3865–3878.
[44] S.C. Wei, J. Yang, Forcing through tumor metastasis: the interplay between tissue rigidity and epithelial–mesenchymal transition, Trends Cell Biol. 26 (2) (2016) 111–120.
[45] J. Zhang, Y. Miao, W. Ni, H. Xiao, J. Zhang, Cancer cell membrane coated silica nanoparticles loaded with ICG for tumour specific photothermal therapy of osteosarcoma, Artif. Cells, Nanomed., Biotechnol. 47 (1) (2019) 2298–2305.
[46] P. Huang, L. Bao, C. Zhang, J. Lin, T. Luo, D. Yang, M. He, Z. Li, G. Gao, B. Gao, S. Fu, D. Cui, Folic acid-conjugated Silica-modified gold nanorods for X-ray/CT imaging-guided dual-mode radiation and photo-thermal therapy, Biomaterials 32 (36) (2011) 9796–9809.
[47] C. Li, Y. Zhang, G. Chen, F. Hu, K. Zhao, Q. Wang, Engineered multifunctional nanomedicine for simultaneous stereotactic chemotherapy and inhibited osteolysis in an orthotopic model of bone metastasis, Adv. Mater. 29 (13) (2017) 1605754.
[48] W. Feng, W. Nie, C. He, X. Zhou, L. Chen, K. Qiu, W. Wang, Z. Yin, Effect of pH-responsive alginate/chitosan multilayers coating on delivery efficiency, cellular uptake and biodistribution of mesoporous silica nanoparticles based nanocarriers, ACS Appl. Mater. Interfaces 6 (11) (2014) 8447–8460.
[49] J. You, P. Zhang, F. Hu, Y. Du, H. Yuan, J. Zhu, Z. Wang, J. Zhou, C. Li, Near-infrared light-sensitive liposomes for the enhanced photothermal tumor treatment by the combination with chemotherapy, Pharm. Res. (N. Y.) 31 (3) (2014) 554–565.
[50] J. You, R. Shao, X. Wei, S. Gupta, C. Li, Near-infrared light triggers release of paclitaxel from biodegradable microspheres: photothermal effect and enhanced antitumor activity, Small 6 (9) (2010) 1022–1031.
[51] Y. Fan, L. Lin, F. Yin, Y. Zhu, M. Shen, H. Wang, L. Du, S. Mignani, J.-P. Majoral, X. Shi, Phosphorus dendrimer-based copper(II) complexes enable ultrasound-enhanced tumor theranostics, Nano Today 33 (2020) 100899.
[52] H. Kim, S. Kim, C. Park, H. Lee, H.J. Park, C. Kim, Glutathione-induced intracellular release of guests from mesoporous silica nanocontainers with cyclodextrin gatekeepers, Adv. Mater. 22 (38) (2010) 4280–4283.